Amorphous Alumina Barrier Coatings on Glass: MOCVD Process and Hydrothermal Aging

*Pierre-Luc Etchepare, Loïc Baggetto, Hugues Vergnes, Diane Samélor, Daniel Sadowski, Brigitte Caussat, and Constantin Vahlas**

Amorphous alumina coatings are applied on the inner surface of glass containers aiming at improving their hydrothermal ageing barrier properties. A direct liquid injection technology is implemented in a metal-organic chemical vapor deposition (MOCVD) process to feed the reactor in a controlled and reproducible way with a solution of aluminum tri-isopropoxide (ATI) in anhydrous cyclohexane. Amorphous alumina coatings are characterized by X-ray diffraction, electron probe microanalysis, scanning electron microscopy, atomic force microscopy and scratch-test method. They are amorphous and hydroxylated at process temperatures between 360 and 420 °C and close to Al_2O_3 stoichiometry between 490 and 560 °C. Hydrothermal ageing simulated by a standard sterilization cycle results in the increase of the root mean square of the surface of the coatings from ≈17 to 61 nm and in the increase of the porosity without affecting the adhesion of the coatings on the glass substrates

1. Introduction

The numerous allotropic phases and tunable crystallinity of alumina make it a major player in many technological and industrial devices. The various properties of alumina coatings match a wide panel of applications such as optical transmittance for optics,[1] insulating properties for microelectronic components,[2] wear resistance,[3] catalyst support,[4] protection against corrosion,[5] and barrier properties.[6] In particular, amorphous alumina coatings present interesting physicochemical characteristics whose nature, extent, and combination depend on the processing conditions.[7,8]

With the aim to process dense, adherent, and durable alumina coatings on metal or polymer substrates various techniques have been tested, such as electron beam evaporation,[9] radio frequency magnetron sputtering,[2] atomic layer deposition,[10] sol–gel,[5] and metalorganic chemical vapor deposition (MOCVD).[7,11–13] CVD is one of the most attractive techniques for the time efficient deposition of such coatings on complex-in-shape geometries with conformal coverage, i.e., uniform thickness along the surface. Composition, stoichiometry, crystallinity, and microstructure of the material can be adjusted by fine tuning of the MOCVD experimental parameters such as reactor design, precursor selection, reactive atmosphere, deposition temperature, and pressure. The MOCVD of alumina from vaporized aluminum tri-isopropoxide (ATI) is very well documented.[7,8,11–16] ATI yields amorphous and stoichiometric alumina coatings with a smooth and dense microstructure at 5 Torr in the temperature range 420 to 650 °C.[7,8,14,15] Higher process temperatures lead to the deposition of nanocrystallized γ-Al_2O_3[15] or to the homogeneous decomposition of ATI, which generates a different microstructure.[11] The ATI molecule is well described in the literature.[17] It is sensitive to water vapor and thus it is subjected to ageing upon exposure to ambient atmosphere, which results in its partial or total hydrolysis in nonvolatile compounds, $Al(O^iPr)_{3-n}(OH)_n$ (n = 1, 2) and $Al(OH)_3$, respectively.[12,17] The precursor is usually melted, maintained in supercooled state, and vaporized with a bubbler.

Despite the simplicity and the cost effectiveness of this solution, the use of ATI in the supercooled state has two drawbacks. First, maintaining ATI at the vaporization temperature for a long-period impacts the stability of the molecule and subsequently the coating quality.[12] Second, it is difficult to know exactly the mass flow rate of the generated reactive gas. Such poorly controlled transport conditions lead to nonreproducible processes, especially for the present case when low activation energy prevails in the entire temperature range of interest, de facto resulting in mass transport limited process. The direct liquid injection (DLI) technology overcomes these drawbacks with the controlled vaporization of the solution made of ATI dissolved in a carrier solvent.[18] The DLI of ATI is insufficiently documented in the literature. Song et al.[19] and Krumdieck et al.[13] implemented the technique in a pulsed-pressure MOCVD process. The authors used a solution of ATI in n-octane and in dry toluene, respectively. Coatings obtained

Dr. P.-L. Etchepare, Dr. L. Baggetto, D. Samélor, D. Sadowski, Dr. C. Vahlas
Centre Interuniversitaire de Recherche et d'Ingénierie des Matériaux
ENSIACET/INPT
Université de Toulouse
Toulouse 31432, France
E-mail: constantin.vahlas@ensiacet.fr
Dr. P.-L. Etchepare, Prof. H. Vergnes, Prof. B. Caussat
Laboratoire de Génie Chimique
ENSIACET/INPT
Université de Toulouse
Toulouse 31432, France

DOI: 10.1002/admi.201600014

between 500 and 550 °C at a nominal base pressure of 0.6 Torr were stoichiometric, amorphous, and presented a nodular surface morphology.

We recently investigated a DLI-MOCVD process for the application of amorphous alumina from ATI on the internal surface of glass bottles. We reported on the process modeling involving the development of a numerical model, using the Computational Fluid Dynamics code FLUENT, to calculate local profiles of gas flow, temperature, concentration, and deposition rates inside the bottle. Interplay between simulation and deposition experiments allowed identifying the process conditions which led to the deposition of transparent coatings with uniform thickness profile.[20,21]

In a continuation of this theoretical work and of recently published preliminary experimental results,[22] we report hereafter on the experimental investigation of the process–structure–property relationship of coatings obtained by the DLI-CVD of ATI. First, we focus on the dissolution of ATI, with the aim to establish criteria for the selection of the different solvents and define a priori the most appropriate one. Then, we detail results on the deposition of alumina coatings on silicon wafers and glass containers. We are especially interested in the possible impact of the solvent on the coatings' composition and characteristics. Finally, we report on the hydrothermal ageing of the alumina coated glass substrates using a standard sterilization cycle in terms of surface morphology and adhesion.

2. Results and Discussion

2.1. Solubility of ATI

The DLI technology requires the dissolution of the precursor in an appropriate solvent to inject and transport the precursor to the deposition area. The selection of the solvent is an important step of the process optimization that has to take into account the physicochemical properties, health and safety characteristics, cost, compatibility with the precursor, and stability of the solvent in the deposition conditions. It is highly preferred that the solvent has the same molecular dipole moments as the precursor to ensure the maximum dissolution. ATI molecule is a tetramer in the solid state. It presents a symmetric so-called "Mitsubishi structure," which corresponds to an apolar molecule, i.e., with a dipole moment equaling 0 debye. Since ATI is better dissolved in apolar solvents, *n*-pentane, cyclohexane, *n*-heptane, and *n*-octane are a priori good candidates for this purpose. They also meet health and safety criteria which exclude carcinogenic, mutagenic and reprotoxic (CMR) substances. A tradeoff was applied for the final selection of the most appropriate solvent based on six criteria. i) The occupational exposure limit value (OELV) at 8 h, which is also related to health and security and depends on national legislations. ii) The melting point, which has to be low enough to avoid solidification of the solvent. iii) The boiling point should be high enough to avoid partial vaporization of the solvent at ambient temperature in the Schlenk flask. iv) The flash point has to be high enough to limit the risk of ignition with air. v) The saturated vapor pressure at the vaporization temperature (200 °C) should be close enough to that of the precursor so as to prevent early vaporization of the solvent. vi) The ratio of the cost between each alkane and the less expensive solvent (cyclohexane) for ≥99% anhydrous quality, which must be the closest possible to one. These criteria were rated in terms of importance as secondary, important, and preponderant and were weighed by a factor of 3, 5, and 8, respectively. This classification favors the preponderant criterion. **Table 1** summarizes the data for each solvent. As for the four criteria, a coefficient of merit was attributed to each value ranging from 1 to 5 for the weaker to the stronger one.

n-Pentane has low boiling point (36.1 °C), flash point (–49 °C), and a high saturated vapor pressure at 200 °C (ratio of 2.07 with ATI), i.e., an important risk of early vaporization. The saturated vapor pressure at 200 °C of *n*-heptane is close to that of ATI (ratio of 1.81); however, its flash point is negative, the OELV is relatively low and the *n*-heptane is relatively more expensive than cyclohexane. *n*-Octane and cyclohexane present

Table 1. Weighed criteria and biological and physicochemical data for four apolar solvents. Melting point, boiling point, and flash point values are extracted from their CAS data sheets, where OELV values come from.[23] Saturated vapor pressure for ATI and the alkanes are calculated from the Antoine's law indicated in ref. [24]. Each value is given a score of merit in parenthesis. The resulting total score for each solvent (last column) is the sum of the products of each weighed criterion times the score of merit. It appears that cyclohexane is the most appropriate solvent to dissolve and transport the ATI.

Criteria	OELV-8 h [ppm]	m.p. [°C]	b.p. [°C]	Flash point [°C]	$\frac{\log(P_{\text{v.s. solv.}})}{\log(P_{\text{v.s. ATI}})}$ at 200 °C	$\frac{\text{Cost(solv.)}}{\text{Cost}(C_6H_{12})}$	Total
Criteria weight	3	3	5	5	5	8	–
n-C_5H_{12}	1000	–129.7	36.1	–49	2.07	1.5	71
	(4)	(5)	(1)	(1)	(2)	(3)	–
C_6H_{12}	200	6.6	80.7	–20	2.14	1	100
	(2)	(3)	(5)	(2)	(2)	(5)	–
n-C_7H_{16}	400	–90.6	98.0	–4	1.81	1.2	95
	(2)	(5)	(5)	(2)	(3)	(3)	–
n-C_8H_{18}	300	–56.8	125.6	13	1.70	5.1	99
	(2)	(5)	(5)	(4)	(5)	(1)	–

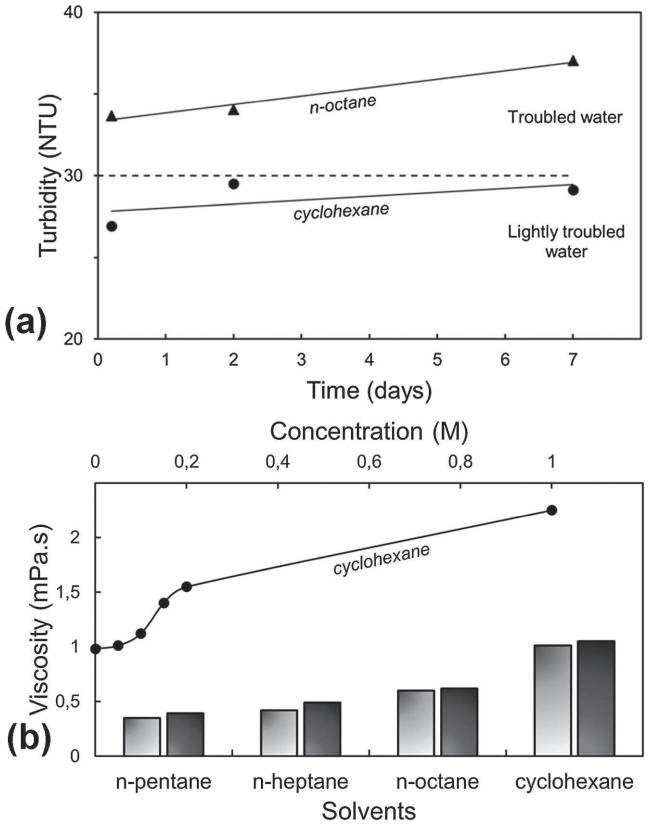

Figure 1. a) Turbidity values of 1 M ATI solutions with cyclohexane (squares) and *n*-octane (circles). Limit value between lightly troubled water and troubled water at 30 nephelometric turbidity units (NTU) is indicated. b) Viscosity of ATI solutions with *n*-pentane, *n*-heptane, *n*-octane, and cyclohexane at 0.05 M fixed concentration (histogram, pure solvents, and solutions in light and dark gray, respectively) and evolution of the viscosity of ATI solutions with cyclohexane as a function of concentration. Solid lines in both diagrams are guide to the eye.

OELV and saturated vapor pressure close to some extent. Although the *n*-octane is more than 5 times more expensive than cyclohexane, its saturated vapor pressure at 200 °C is near that of ATI, and its boiling and flash points are high. Preliminary conclusions from this investigation reveal that either cyclohexane or *n*-octane can be selected to dissolve and transport the ATI. However, additional criteria, such as viscosity and turbidity, dealing with the solubility of ATI per se should be considered to select the most appropriate alkane.

The histogram of **Figure 1**a shows the viscosity of the four solvents and of the corresponding solutions of ATI at 0.05 M fixed concentration, which is typical for an injected solution in a DLI-MOCVD process. The viscosity of the four solvents is low, not exceeding that of water (1 mPa s at 20 °C). Viscosities of the solutions are almost equal to those of pure solvents; they are compatible with the DLI technology and are too close to each other to allow discrimination. Figure 1b shows the evolution of the turbidity of 1 M solutions of ATI in cyclohexane and *n*-octane for comparison as a function of their ageing up to 7 d. It is worth noting that 1 M concentration and 7 d ageing are relatively high values for a CVD process. The turbidity of both solutions increases with ageing. That of the solutions with cyclohexane is systematically lower, revealing a higher stability than the one with *n*-octane.

Finally, the evolution of the viscosity of the ATI/cyclohexane solution as a function of concentration up to 1 M is shown in Figure 1. The viscosity increases from 0.98 mPa s at 0.05 M up to 2.25 mPa s at 1 M, i.e., to a value which is still convenient for DLI. A global consideration of these results reveals that cyclohexane is the most appropriate solvent for ATI. An additional screening of the possible solvents is that they must not be subjected to thermal or reactive decomposition during deposition resulting in the pollution of the coating. This criterion requires dedicated experimental investigation and is out of the scope of the present work.

2.1. Composition and Morphology of Amorphous Alumina Coatings

X-ray diffraction (XRD) patterns of coatings deposited on Si do not show any peaks associated with the formation of a crystalline structure for all deposition temperatures,[21] which indicates the coatings are all amorphous. **Figure 2**a shows the evolution of the O/Al atomic ratio and carbon concentration in the coatings deposited on Si, as a function of deposition temperature, determined by electron probe microanalysis (EPMA) and X-ray photoelectron spectroscopy (XPS), respectively. The coatings grown onto Si substrates inside the horizontal MOCVD reactor (blue dots) prepared at 360 and 420 °C show O/Al atomic ratios equal to 2.12 and 1.80, respectively. These values correspond to compositions close to AlOOH (atomic ratio 2.0) and partially hydroxylated $AlO_{1+x}(OH)_{1-2x}$ coatings. Coatings prepared at 490 and 560 °C show O/Al ratios equal to 1.53 and 1.57, respectively, in close agreement with the formula Al_2O_3 (atomic ratio 1.5). Coatings deposited in the vertical MOCVD reactor (Figure 2a, red dots) present O/Al ratios of 1.88 and 1.56 at 420 and 600 °C, respectively, in good agreement with those measured for the coatings grown in the horizontal MOCVD reactor. Hence, it appears that the inlet ATI molar fraction and the reactor configuration used here have little influence on the coating composition. The C content (Figure 2a, black dots) measured by XPS for coatings deposited on Si substrates in the horizontal reactor after ≈100 nm surface erosion is below 1 at% for all temperatures, similar to the C content measured by EPMA on coatings grown in the vertical reactor (Figure 2a, white dots). Gleizes et al. measured similar O/Al atomic ratio (EPMA) for alumina coatings deposited by MOCVD with vaporized ATI in the temperature range of 480–600 °C.[15] The evolution of the elemental composition with deposition temperature observed by EPMA was further investigated using XPS (Figure 2b). The amount of aliphatic carbon (C–C and C–H bonds only) is less than 1 at% and likely results from small amounts of solvent residue incorporated in the coating during growth.

The Al2p signal apparently shows a single symmetric peak corresponding to Al^{3+} in an O^{2-} framework. The signals for Al2p in Al_2O_3, AlOOH, and $Al(OH)_3$ are very close in binding energy and consequently, they are hard to separate.[25] The O1s signal is a better discriminant for the presence of hydroxyl groups, which have a peak expected at ≈1.3 eV off the main O^{2-} peak of

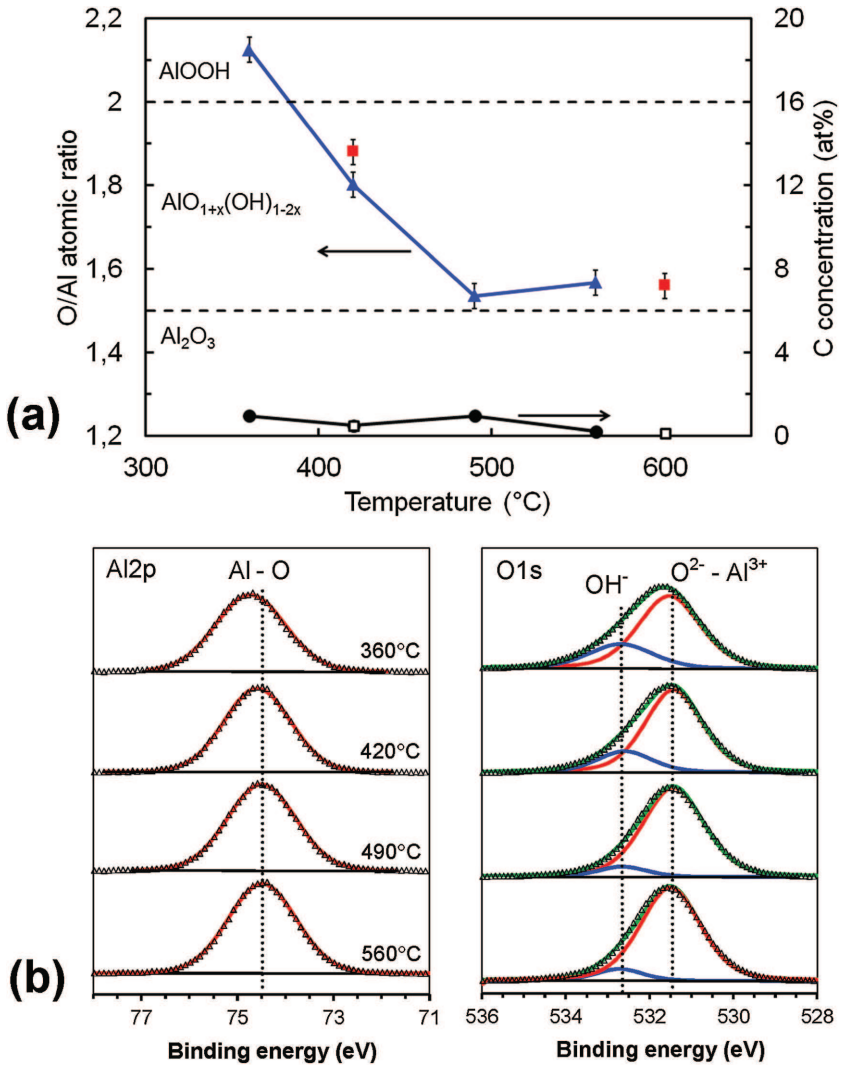

Figure 2. a) Elemental composition of alumina coatings grown on Si substrates. O/Al atomic ratios were measured using EPMA for coatings processed in the horizontal (blue dots) and vertical (red dots) reactors. Carbon concentration was determined by XPS for coatings deposited on Si substrates in the horizontal reactor (black dots) and by EPMA for those prepared in the vertical reactor on glass bottles (white dots). b) High resolution XPS spectra (Al2p and O1s) of alumina coatings deposited on Si substrates at 360, 420, 490, and 560 °C. The decomposition of the spectra into the assigned chemical species is shown for each core level. Red and blue curves are for the oxide and hydroxide species, respectively.

Al_2O_3.[25] The measured O1s signals clearly show a main peak around 531.4 eV at the location expected for O^{2-} in the Al_2O_3 framework,[26] which is accompanied with a shoulder around 532.7 eV of increasing intensity with decreasing temperature, attributable to hydroxyl groups. The relative amount of hydroxyl groups increases with decreasing temperature, in agreement with the increasing O/Al ratio measured with EPMA. However, the response related to hydroxyls groups is not as intense as expected for a composition close to AlOOH obtained at 360 °C. This discrepancy likely results from ion beam damage, which decreases the actual quantity of OH signal. Nonetheless, the resulting spectra show a reasonable trend with the EPMA data. This is confirmed, for instance, in the case of the coatings deposited at 490 and 560 °C which show the persistence of OH groups.

The coating morphology is shown in the cross section SEM micrographs in **Figure 3**. The coating surface is smooth but slightly porous with nanosized cavities over the entire height (Figure 3b), in contrast with alumina coatings deposited from vaporized ATI which are very smooth and dense.[27] This particular morphology is attributed to the presence of cyclohexane in the DLI process possibly resulting from steric hindrance during the coating growth.

2.3. Chemical Durability of Coatings Grown on the Inner Walls of Glass Containers after Steam Sterilization

The evolution of the surface morphology and adhesion of the coating on glass substrates in a steam sterilization cycle in a warm and wet atmosphere was investigated. SEM micrographs of alumina coatings grown on glass container surfaces, before and after sterilization cycle, are presented in **Figure 4**. Before the hydrothermal ageing, the coating looks relatively rough and presents in cross section (Figure 4c) a columnar structure. This morphology can be compared with those of alumina coatings deposited on Si substrate and shown in Figure 3. The lighter layer at the interface between the glass surface and the alumina coating can be attributed to the tin oxide coating deposited on glass bottle during the manufacturing process, with the aim to improve the mechanical properties. After a sterilization cycle, the coating presents two parts with different microstructures. The coating surface is significantly rougher and porous with submicrometric cavities, while the layer at the interface with the glass substrate is denser and is a priori not damaged. Surface 3D topography AFM images of alumina coatings deposited on glass containers before and after a sterilization cycle are shown in **Figure 5**. Results of measured roughness for uncoated and coated containers are summarized in **Table 2**. The root-mean-square (RMS) average of the roughness of the bare containers is low (0.3 and 0.7 nm), i.e., the glass surface prior to deposition is extremely flat and smooth despite a slight increase of the surface roughness after the sterilization cycle. Before the sterilization cycle, alumina coatings display somewhat rough features with a mean RMS value 17.1 nm. The sterilization cycle yields a strong increase of the roughness value to 61.7 nm, which confirms the observation of the surface and cross section of the coating in Figure 4. It demonstrates the increase of surface porosity

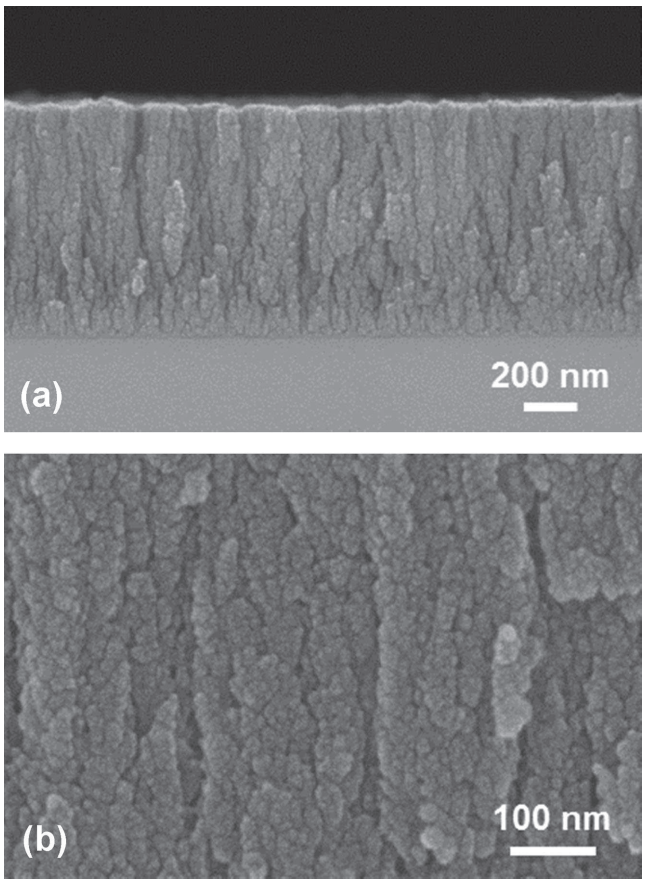

Figure 3. Cross-section SEM micrographs of an amorphous alumina coating deposited on Si substrate at a deposition temperature of 480 °C at a) low and b) high magnifications.

and subsequent coating deterioration by dissolution. From the SEM and AFM observations it can be concluded that ageing in such wet and hot environment damages the coating surface, making it more rough and porous.

The effect of a sterilization cycle on the adhesion of the coating on glass was investigated by scratch-testing. SEM images of the tracks are presented in **Figure 6** before and after the sterilization. These micrographs reveal the features of four different coating failure modes. In the as-processed sample, the Hertzian cracking mode is determined by the presence of the indenter mark, i.e., the first circular crack on the coating surface. This cracking mode witnesses the stress relaxation induced beneath the loaded indenter. It corresponds to a through-thickness cracking of a hard coating (compressive stresses generated ahead of the indenter and tensile stresses behind it). Tensile cracking failure mode is also found in the literature for alumina coatings deposited on glass substrate.[28] The feature of the second cracking mode is the propagation of radial chevron cracks, which are 45° from the direction of the scratch. The third mode occurs with the coating chipping and substrate exposure.[29] This mode is related to the coating adhesion. An energy dispersive spectrometry analysis confirms the presence of the bare glass on the edges of the track, hence supporting the total coating delamination.

An additional mode is observed for sterilized coated containers with partial delamination or radial (chevron) cracks on the track edges at low loads and before the Hertzian cracking mode. The critical loads were measured at the beginning of each cracking failure mode and are given in **Table 3**. Comparison of critical loads among samples from different studies is only allowed if the coating-substrate system, the coating thickness, the scratch-test apparatus, the scratch parameters, and the applied load are the same.

For the sterilized coated container, the additional radial cracking mode on the track edge mode occurs for a mean load of 11.9 ± 2.3 N, far before the Hertzian cracking mode (22.2 ± 2.9 N). The critical loads for the Hertzian cracking mode (22.2 ± 2.9 N) and the radial cracking mode (24.1 ± 1.0 N) are higher for the sterilized coated bottle than the as-processed system (respectively 12.2 ± 3.5 N and 16.8 ± 2.0 N). The chipping mode occurs at relatively high loads (25.5 ± 1.7 N and 27.5 ± 1.7 N), which should lead to a satisfactory adhesion of the coating. Moreover, the measured critical loads for the chipping mode are similar for the coated container before and after the sterilization cycle.

These results suggest that the sterilized alumina coating presents two layers with different features. The upper part of the coating is damaged by partial dissolution during the sterilization cycle, making it porous, rough and brittle, which can explain why an additional cracking mode occurs. For low loads, the indenter makes a scratch on the corroded surface and generates radial cracks on the track edges, then sinks into the coating. The deeper layer remains unaffected by the hydrothermal ageing and is hard and dense. The same values of critical loads for the chipping mode measured in both cases could indicate that the adhesion of the deeper layer is not altered by the sterilization cycle.

3. Conclusions

Alumina coatings were deposited by DLI-MOCVD from ATI precursor at 5 Torr. Direct liquid injection technology generally allows a better control of generated reactive gaseous mass flow and vaporization, thereby contributing to a more robust process. Cyclohexane was selected to dissolve and transport ATI to the deposition area. A very low amount of carbon (below 1 at%) is found in the coating composition, which proves the solvent does not readily decompose during deposition. Coatings are amorphous in the temperature range 360–560 °C. Coatings processed at high temperatures (490–560 °C) are close to stoichiometric Al_2O_3 with a very low amount of hydroxyl groups; the composition of the coatings deposited at lower temperatures (360–420 °C) ranges from AlOOH to partially hydroxylated alumina $AlO_{1+x}(OH)_{1-2x}$ with increasing temperature. The as-prepared coating morphology is relatively smooth (RMS 17.1 nm) and slightly porous with nanometer cavities. Amorphous alumina coatings were deposited on the inner surface of glass containers and underwent a steam sterilization cycle in a warm and wet atmosphere. SEM observation and AFM imaging show that the sterilization cycle affects the surface topography and morphology, making the coating rougher

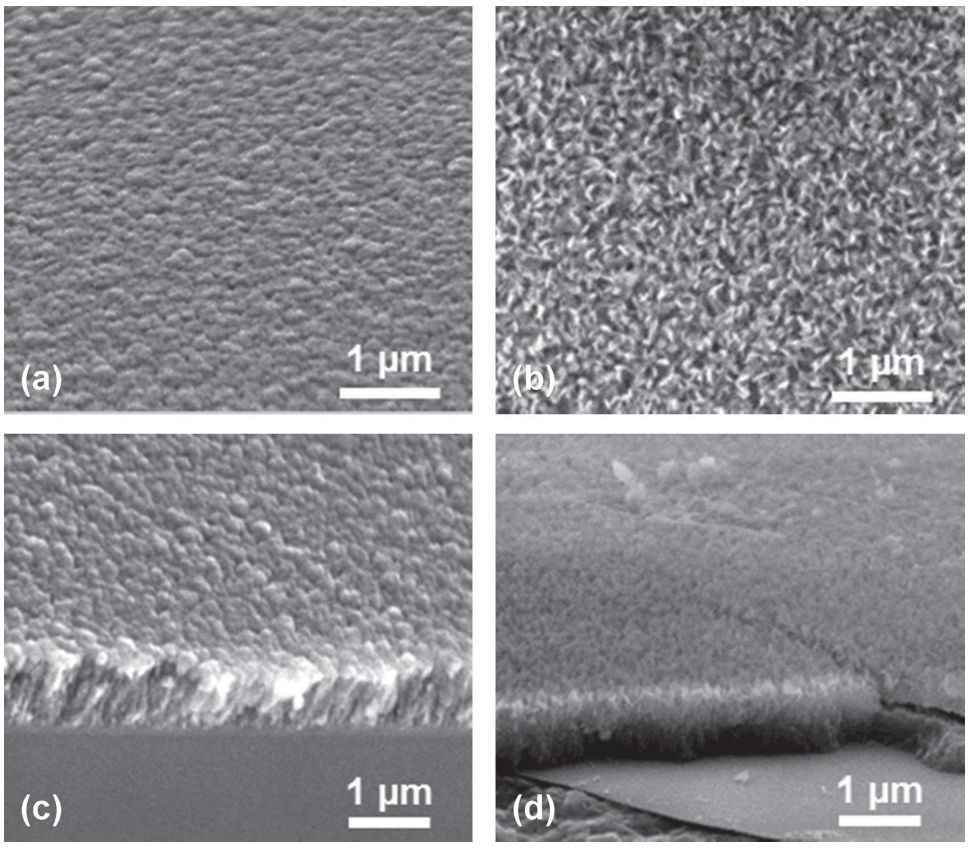

Figure 4. Surface (top) and cross section (bottom) SEM micrographs of amorphous alumina deposited at 480 °C on glass containers a, c) before and b, d) after a sterilization cycle. The flat part seen in Figure d is a bit of the glass bottle.

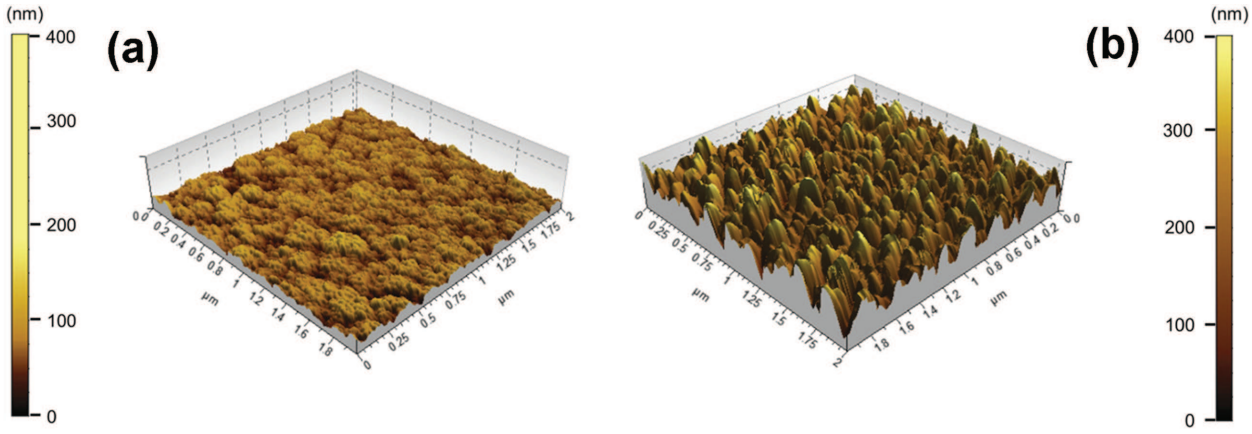

Figure 5. 3D topography images of the surfaces measured by AFM employing the Tapping mode for amorphous alumina coatings on the inner walls of glass containers a) before and b) after a sterilization cycle. Note that the height scales are identical. Scanned surface area is 2×2 µm^2.

Table 2. Measured roughness of uncoated and coated containers before and after a sterilization cycle during 1 h at 121 °C.

	Uncoated containers		Coated containers	
	As-processed	Sterilized	As-processed	Sterilized
Roughness RMS (nm)	0.3	0.7	17.1	61.7

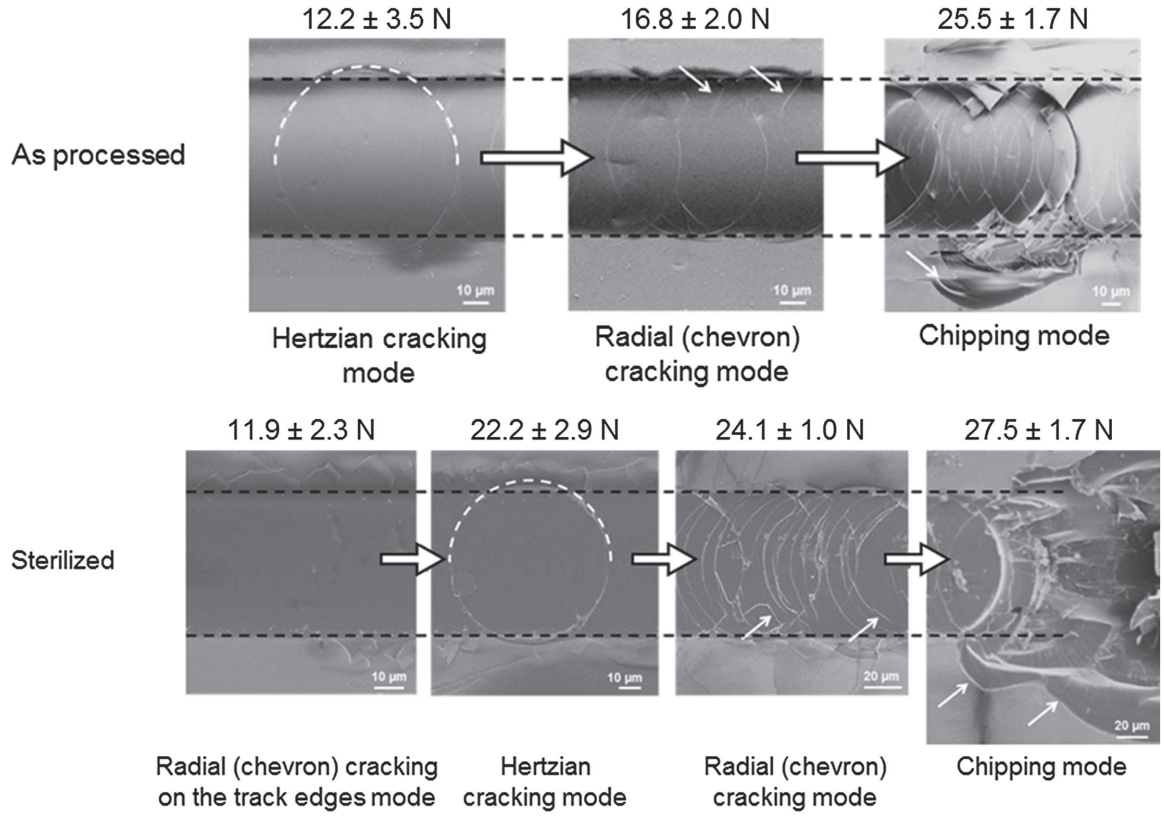

Figure 6. SEM micrographs of scratch tracks on the surface of alumina coating deposited on glass containers at 480 °C as processed. Cracking failure modes depend on the indenter load. They are defined as Hertzian cracking mode, radial (chevron) cracking mode, and chipping mode for as-processed samples, and as buckling/recovery spallation mode, Hertzian cracking mode, radial (chevron) cracking mode, and chipping mode for sterilized ones. Dotted semicircle lines and arrows are guides to the eye.

(RMS 61.7 nm) and more porous. However, scratch-tests reveal that the coating adhesion on the glass surface is not affected by the hydrothermal ageing.

4. Experimental Section

The precursor solution was prepared by mixing ATI (98%, Acros Organics) and preferably anhydrous cyclohexane (99.5%, $H_2O < 10$ ppm, Acros Organics), or *n*-pentane (≥99%, Sigma Aldrich), *n*-heptane (≥99%, Sigma Aldrich), or *n*-octane (98%, Acros Organics), inside a Schlenk flask. The viscosity of 0.05 to 1 M solutions of ATI in cyclohexane and 0.05 M solutions of ATI in *n*-pentane, *n*-heptane, and *n*-octane was measured with a falling sphere viscometer. The turbidity, i.e., the presence of insoluble particles in the solvent was measured for highly concentrated solutions in cyclohexane and *n*-octane by the nephelometry method employing a Hach 2100 instrument. ATI powder was weighed and sealed in a Schlenk flask inside a glovebox circulated with purified Ar (99.9997%, Air Products). The sealed flask was filled outside of the glovebox with the appropriate quantity of anhydrous cyclohexane using an airtight, Ar-purged, glass syringe to prepare a solution of varying concentration from 0.025 to 1 M. Then, the Schlenk flask was connected with the injection system and purged several times with pressurized N_2 (99.9999%, Praxair). DLI of the solution was carried out with Kemstream Vapbox systems. One gas line was connected to the injection system consisting of an N_2-pressurized Schlenk flask filled with the precursor solution and connected to a set of two injectors. During the deposition, the ATI solution was injected through an injector to form small droplets with a calculated flow rate from 0.90 to 1.55 mL min^{-1}. The frequency (2 or 3 Hz) and opening times (from 3 to 30 ms) of the injection system were controlled by a computer interface. The injected solution was blended in the mixing chamber with carrier gas (pure N_2) with a pressure differential held at 1 bar. The mixing carrier gas flow of N_2 was fixed at a flow rate of 300 standard cubic centimeters per minute (sccm).

Glass containers (42.5 mm diameter, 73 mm height bottles) and Si substrates (10 × 10 mm, cut from 4″ Si (100) wafers (Sil'tronix)) were cleaned in an ultrasonic bath with acetone and ethanol. DLI-MOCVD was performed in two different reactors.

Table 3. Critical load of coating failure modes determined with the scratch-test method for as-processed and sterilized coated glass containers.

	Critical load [N]			
	Radial (chevron) cracking on the track edges mode	Hertzian cracking mode	Radial (chevron) cracking mode	Chipping mode
As-processed	–	12.2 ± 3.5	16.8 ± 2.0	25.5 ± 1.7
Sterilized	11.9 ± 2.3	22.2 ± 2.9	24.1 ± 1.0	27.5 ± 1.7

Deposition onto Si substrates was carried out using a horizontal hot-wall reactor composed of a quartz tube (25 mm diameter, 300 mm length) heated by a resistive furnace. Samples were placed on a stainless steel (SS) holder in the center of the quartz tube where the temperature was uniform. The total flow rate of the carrier gas with vaporized solution was maintained unchanged at 814 sccm. The inlet ATI molar fraction was estimated to be 8.2×10^{-3}.

Deposition on the inner walls of glass containers was performed in a vertical hot-wall DLI-MOCVD reactor, as described in detail elsewhere.[20] It is recalled that the reactive gas phase was driven with pure N_2 and introduced through a SS nozzle from the upper part of the quartz tube. In this configuration, the total flow rate and the inlet ATI molar fraction were equal to 585 sccm and 1.7×10^{-3}, respectively. A SS holder maintained the glass container in the gas feeding tube axis. An inductively heated thermoregulated SS cylinder around the reaction chamber ensured a temperature profile along the container with a set temperature at the bottom external surface on the central axis of the container 480 °C.[19]

Both systems are hot-wall reactor with comparable quartz tube dimensions. DLI devices come from the same supplier and are almost equivalent. The vaporization chamber and SS transport lines were thermally regulated to allow efficient flash vaporization of the mixture droplets without early ATI decomposition or partial solvent vaporization. Dry pumps (base pressure $< 5 \times 10^{-2}$ Torr) and pressure gauges connected to the output of the deposition chambers were used to control the reaction pressure to 5 Torr.

Coated glass containers were submitted to one sterilization cycle in the wet atmosphere. Samples were filled with ultrapure water (18.2 MΩ cm) and placed for 1 h inside an autoclave (Getinge) operating at 121 °C and 2 bar absolute pressure. Heating and cooling rates were controlled to avoid thermal cracks.

XRD was performed on a Bruker D8 Advance using a Cu Kα (1.5418 Å) X-ray tube operated at 40 kV and 40 mA, an Ni filter and solid-state Lynxeye detector in θ–3°/θ+3° configuration. Samples were measured on a zero background holder and a θ offset of 3° was applied on the X-ray source and detector arms to suppress the strong diffraction of the Si substrates.

XPS was performed on a Thermo Scientific K-Alpha instrument capable of a typical base pressure of 10^{-9} Torr using monochromatic Al Kα (1486.7 eV). The spectrometer energy calibration was performed using the Au4f7/2 (83.9 ± 0.1 eV) and Cu2p3/2 (932.7 ± 0.1 eV) photoelectron lines. Charging compensation and neutralization were applied by using a dual beam flood gun. The probed areas were about 400 µm in diameter. Surface erosion was employed using Ar ions accelerated at 2 kV, resulting in an erosion rate of about 0.08 nm s^{-1}. Constant pass energy of 30 eV and energy steps of 0.1 eV were used for high resolution scans. The photoelectron peaks were analyzed by Gaussian/Lorentzian (G/L = 70/30) peak fitting and using a Shirley background. The atomic concentrations were determined from photoelectron peak areas using the atomic sensitivity factors reported by Scofield,[30] taking into account the transmission function of the analyzer calculated at different pass energies from Ag3d and AgMNN peaks collected for a reference sample.

The O/Al ratios in the coatings were determined by EPMA with a Cameca SXFive apparatus operated at 10 and 15 keV and calibrated using a high purity alumina standard. Samples were covered by a thin layer of carbon in a vaporization chamber (Leica) to prevent charging effects. Each sample was measured 12 times in different locations to determine the spatial homogeneity of the sample composition.

SEM on coated glass container fragments was performed with a LEO 435VP instrument. Samples were fractured and metalized with silver and graphite before analysis in order to avoid charging effects. Acquisition was performed with an acceleration voltage of 10 kV, a probe current between 40 and 80 pA and a working distance 11 mm. SEM on alumina coatings deposited on Si substrates was performed with a JEOL JSM-7800F field emission scanning electron microscope operated at 10 kV in backscattered mode. Samples were fractured and metalized with platinum or silver before imaging.

The roughness of the alumina coatings deposited on the glass surface, before and after the sterilization cycle, was measured by AFM in tapping mode using an Agilent 5500 instrument. The probe silicon tip (AppNano ACT-50) with a spring constant of 13–77 N m^{-1} and resonance frequency between 200 and 40 kHz scanned areas of samples with a scan rate of 2 µm s^{-1} with 256 × 256 data points. Pico Image software (Agilent Technology) was used to analyze and process the data.

The adhesion of alumina coatings on glass containers before and after the sterilization cycle was investigated by scratch-test method (standard EN 1071) using a CSM Revetest Instruments. Samples were scratched using a diamond indenter with a spherical tip of 200 µm and a cone angle of 120° at a constant loading rate of 15 N min^{-1}. The load applied on the coating surface increased from 1 to 30 N. The scratch track was fixed at 4 mm.

Acknowledgements

The authors are indebted to Viviane Turq, Djar Oquab, Yannick Thebault, Cedric Charvillat, and Jérôme Esvan, CIRIMAT, for helping with scratch-testing, SEM, AFM, XRD, and XPS measurements, to Philippe de Parseval, UMS Castaing, for the EPMA characterization, and to Florent Colomes and Iulian Stan for the experimental study of ATI solubility. The authors also thank Hervé Guillon (Kemstream, Montpellier) for providing useful advices on the operation of the DLI facility. L.B. acknowledges the STAE-RTRA Foundation (Toulouse, France) for the financial support within the RTRA-STAE/2014/P/VIMA/12 project grant framework.

[1] D.-H. Kuo, B.-Y. Cheung, R.-J. Wu, *Thin Solid Films* **2001**, *398*, 35.
[2] M. Voigt, M. Sokolowski, *Mater. Sci. Eng. B* **2004**, *109*, 99.
[3] R. M'Saoubi, S. Ruppi, *CIRP Annals–Manuf. Technol.* **2009**, *58*, 57.
[4] K. Haas-Santo, M. Fichtner, K. Schubert, *Appl. Catal. A* **2001**, *220*, 79.
[5] J. Masalski, J. Gluszek, J. Zabrzeski, K. Nitsch, P. Gluszek, *Thin Solid Films* **1999**, *349*, 186.
[6] C. F. Struller, P. J. Kelly, N. J. Copeland, C. M. Liauw, *J. Vac. Sci. Technol. A* **2012**, *30*, 041502.
[7] D. Samélor, A. M. Lazar, M. Aufray, C. Tendero, L. Lacroix, J. D. Béguin, B. Caussat, H. Vergnes, J. Alexis, D. Poquillon, N. Pébère, A. Gleizes, C. Vahlas, *J. Nanosci. Nanotech.* **2011**, *11*, 8387.
[8] D. Samélor, M. Aufray, L. Lacroix, Y. Balcaen, J. Alexis, H. Vergnes, D. Poquillon, J. D. Beguin, N. Pébère, S. Marcelin, B. Caussat, C. Vahlas, *Adv. Sci. Technol.* **2010**, *66*, 66.
[9] L. Wu, L. Song, J. Wu, L. Zhao, C. Jiang, *Ceram. Int.* **2007**, *33*, 747.
[10] a) M. D. Groner, F. H. Fabreguette, J. W. Elam, S. M. George, *Chem. Mater.* **2004**, *16*, 639; b) M. K. Tripp, C. Stampfer, D. C. Miller, T. Helbling, C. F. Herrmann, C. Hierold, K. Gall, S. M. George, V. M. Bright, *Sensor and Actuator* **2006**, *130*, 419.
[11] S. Blittersdorf, N. Bahlawane, K. Kohse-Höinghaus, B. Atakan, J. Müller, *Chem. Vap. Dep.* **2003**, *9*, 194.
[12] M. M. Sovar, D. Samélor, A. N. Gleizes, C. Vahlas, *Surf. Coat. Technol.* **2007**, *201*, 9159.
[13] S. Krumdieck, S. Davies, C. M. Bishop, T. Kemmitt, J. V. Kennedy, *Surf. Coat. Technol.* **2013**, *230*, 208.
[14] A. Gleizes, M. M. Sovar, D. Samélor, C. Vahlas, *Adv. Sci. Technol.* **2006**, *45*, 1184.
[15] A. Gleizes, C. Vahlas, M. M. Sovar, D. Samélor, M. C. Lafont, *Chem. Vap. Dep.* **2007**, *13*, 23.
[16] a) R. W. J. Morssinkhof, The deposition of thin alumina films on steels by MOCVD, *University of Twente, The Netherlands* **1991**;

b) S. K. Soni, D. Samélor, B. W. Sheldon, C. Vahlas, A. N. Gleizes, *ECS Trans.* **2009**, *25*, 1309; c) H. Vergnes, D. Samelor, A. Gleizes, C. Vahlas, B. Caussat, *Chem. Vap. Dep.* **2011**, *17*, 181.
[17] N. Y. Turova, V. A. Kozunov, A. I. Yanovskii, N. G. Bokii, Y. T. Struchkov, B. L. Tarnopol'skii, *J. Inorg. Nucl. Chem.* **1979**, *41*, 5.
[18] a) M. Manin, S. Thollon, F. Emieux, G. Berthome, M. Pons, H. Guillon, *Surf. Coat. Technol.* **2005**, *200*, 1424; b) J. Mungkalasiri, L. Bedel, F. Emieux, J. Doré, F. N. R. Renaud, F. Maury, *Surf. Coat. Technol.* **2009**, *204*, 887.
[19] M.-K. Song, S.-W. Kang, S.-W. Rhee, *J. Electroch. Soc.* **2005**, *152*, C108.
[20] P.-L. Etchepare, H. Vergnes, D. Samélor, D. Sadowski, C. Brasme, B. Caussat, C. Vahlas, *Adv. Sci. Technol.* **2014**, *91*, 117.
[21] P.-L. Etchepare, H. Vergnes, D. Samélor, D. Sadowski, B. Caussat, C. Vahlas, *Surf. Coat. Technol.* **2015**, *275*, 167.
[22] P.-L. Etchepare, L. Baggetto, H. Vergnes, D. Samélor, D. Sadowski, B. Caussat, C. Vahlas, *Phys. Stat. Sol. C* **2015**, *12*, 944.
[23] B. Courtois, S. Cadou, Vol. ED *984*, INRS, Paris **2012**.
[24] a) R. H. T. Bleyerveld, W. Fieggen, H. Gerding, *Rec. Trav. Chim. Pays-Bas* **1972**, *91*, 477; b) ed. in *Chemical Properties Handbook*, C. L. Yaws, McGraw-Hill Education, New York **1999**.
[25] a) H. He, K. Alberti, T. L. Barr, J. Klinowski, *J. Phys. Chem.* **1993**, *97*, 13703; b) A. Hess, E. Kemnitz, A. Lippitz, W. E. S. Unger, D. H. Menz, *J. Catal.* **1994**, *148*, 270; c) J. T. Kloprogge, L. V. Duong, B. J. Wood, R. L. Frost, *J. Colloid Interf. Sci.* **2006**, *296*, 572.
[26] a) L. Baggetto, N. J. Dudney, G. M. Veith, *Electrochim. Acta* **2013**, *90*, 135; b) S. Verdier, L. El Ouatani, R. Dedryvère, F. Bonhomme, P. Biensan, D. Gonbeau, *J. Electroch. Soc.* **2007**, *154*, A1088.
[27] Y. Balcaen, N. Radutoiu, J. Alexis, J. D. Béguin, L. Lacroix, D. Samelor, C. Vahlas, *Surf. Coat. Technol.* **2011**, *206*, 1684.
[28] C. H. Lin, H. L. Wang, M. H. Hon, *Thin Solid Films* **1996**, *283*, 171.
[29] a) S. J. Bull, *Surf. Coat. Technol.* **1991**, *50*, 25; b) S. J. Bull, *Tribol. Int.* **1997**, *30*, 491.
[30] J. H. Scofield, *J. Electron Spec. Rel. Phen.* **1976**, *8*, 129.